Published in final edited form as:
Nat Chem. 2009 September 23; 1: 568–572. doi:10.1038/nchem.366.

Geometric and Electronic Structure and Reactivity of a Mononuclear "Side-On" Nickel(III)-Peroxo Complex

Jaeheung Cho[1], **Ritimukta Sarangi**[2], **Jamespandi Annaraj**[1], **Sung Yeon Kim**[1], **Minoru Kubo**[3], **Takashi Ogura**[3], **Edward I. Solomon**[2,4,*], and **Wonwoo Nam**[1,*]

[1]Department of Chemistry and Nano Science, Department of Bioinspired Science, Center for Biomimetic Systems, Ewha Womans University, Seoul 120-750, Korea

[2]Stanford Synchrotron Radiation Laboratory, SLAC National Accelerator Laboratory, Menlo Park, CA 94025, USA

[3]Picobiology Institute, Graduate School of Life Science, University of Hyogo, Hyogo 678-1297, Japan

[4]Department of Chemistry, Stanford University, Stanford, CA 94305, USA

Abstract

Metal-O_2 adducts, such as metal-superoxo and -peroxo species, are key intermediates often detected in the catalytic cycles of dioxygen activation by metalloenzymes and biomimetic compounds. The synthesis and spectroscopic characterization of an end-on nickel(II)-superoxo complex with a 14-membered macrocyclic ligand was reported previously. Here we report the isolation, spectroscopic characterization, and high-resolution crystal structure of a mononuclear side-on nickel(III)-peroxo complex with a 12-membered macrocyclic ligand, $[Ni(12\text{-}TMC)(O_2)]^+$ (**1**) (12-TMC = 1,4,7,10-tetramethyl-1,4,7,10-tetraazacyclododecane). Different from the end-on Ni(II)-superoxo complex, the Ni(III)-peroxo complex is not reactive in electrophilic reactions, but is capable of conducting nucleophilic reactions. The Ni(III)-peroxo complex transfers the bound dioxygen to manganese(II) complexes, thus affording the corresponding nickel(II) and manganese(III)-peroxo complexes. The present results demonstrate the significance of supporting ligands in tuning the geometric and electronic structures and reactivities of metal-O_2 intermediates that have been shown to have biological as well as synthetic usefulness in biomimetic reactions.

Metalloenzymes activate dioxygen to carry out a variety of biological reactions including biotransformation of naturally occurring molecules, oxidative metabolism of xenobiotics, and oxidative phosphorylation. One goal in biomimetic research is to understand the mechanistic details of dioxygen activation and oxygenation reactions and the structures of reactive intermediates occurring at the active sites of the metalloenzymes[1]. In the unified mechanism of dioxygen activation, dioxygen first binds to a reduced metal center that forms metal-superoxo and -peroxo intermediates, followed by O-O bond cleavage leading to the formation of high-valent metal-oxo species that are believed to carry out substrate oxidations[1]. Among the metal-oxygen intermediates, mononuclear metal-O_2 adducts, such

*Corresponding authors: wwnam@ewha.ac.kr, edward.solomon@stanford.edu. Correspondence and requests for materials should be addressed to W.N.

Author contributions: J.C., E.I.S., and W.N. conceived and designed the experiments; J.C., R.S., J.A., S.Y.K., and M.K. performed the experiments; J.C., R.S., J.A., M.K., and T.O. analyzed the data; J.C., R.S., E.I.S., and W.N. co-wrote the paper.

Additional information: Supplementary information and chemical compound information accompany this paper at www.nature.com/naturechemistry. Reprints and permission information is available online at http://npg.nature.com/reprintsandpermissions/

as metal-superoxo and -peroxo species, have attracted much attention as key intermediates in the catalytic cycles of dioxygen activation by metalloenzymes, including heme and non-heme iron and copper enzymes[2-4]. In biomimetic and synthetic chemistry, mononuclear metal-O_2 complexes, including titanium, vanadium, chromium, manganese, iron, cobalt, nickel, copper, and the second and third row transition metals, have been synthesized and characterized with various spectroscopic techniques and X-ray crystallography, and their reactivities have been extensively investigated in nucleophilic and electrophilic oxidation reactions[5-11]. A notable example is the mononuclear copper-O_2 species, which shows a diverse and rich chemistry in structures, spectroscopic properties, and reactivities[10-16]. X-ray crystal structures of side-on (η^2) and end-on (η^1) Cu(II)-superoxo and side-on (η^2) Cu(III)-peroxo complexes were successfully obtained[17-19], and the mode of O_2 coordination (e.g., side-on vs end-on O_2-binding) and the electronic nature of the Cu-O_2 core (e.g., Cu(II)-superoxo vs Cu(III)-peroxo) were found to vary depending on the supporting ligands of copper complexes[20-23].

In the case of mononuclear Ni-O_2 intermediates, side-on and end-on nickel(II)-superoxo and side-on nickel(II)-peroxo complexes have been characterized by spectroscopic, X-ray crystallographic, and computational methods[24-27], and the Ni(II)-superoxo complexes showed electrophilic reactivity, such as the oxidation of PPh_3 to $OPPh_3$[24-26]. However, to the best of our knowledge, the crystal structure and reactivity of a mononuclear Ni(III)-peroxo complex have not yet been reported. In this study, we have examined the effects of supporting ligands on the mode of O_2 coordination and the electronic structure of the Ni-O_2 moiety in mononuclear Ni-O_2 complexes, by varying the ring–size of a macrocyclic ligand coordinated to $[Ni(II)(14\text{-}TMC)(O_2)]^+$ (**2**) (14-TMC = 1,4,8,11-tetramethyl-1,4,8,11-tetraazacyclotetradecane) that was characterized as an end-on Ni(II)-superoxo complex by spectroscopic and computational methods[25]. We now report for the first time the synthesis, spectroscopic and electronic properties, and crystal structure of a mononuclear side-on (η^2) nickel(III)-peroxo complex stabilized by a 12-membered macrocyclic ligand, $[Ni(III)(12\text{-}TMC)(O_2)]^+$ (**1**) (12-TMC = 1,4,7,10-tetramethyl-1,4,7,10-tetraazacyclododecane). The reactivities of the Ni(III)-peroxo complex in electrophilic and nucleophilic reactions and peroxo group transfer to other metal complexes have been discussed as well.

Results and discussion

The starting nickel complex, $[Ni(12\text{-}TMC)(CH_3CN)]^{2+}$ (**3**), was synthesized and characterized with UV-vis absorption spectroscopy, electrospray ionization mass spectrometry (ESI MS), and X-ray crystallography (see Supplementary text, Figs. S1 and S2, Tables S1 and S2). The reaction of **3** with 5 equiv H_2O_2 in the presence of 2 equiv triethylamine (Et_3N) in CH_3CN at 0 °C produces a green intermediate, **1**, that exhibits distinct absorption features that are different from those of **2** (Fig. 1)[25]. The intermediate persisted for several days at 25 °C, and the greater thermal stability of **1** allowed us to isolate crystals that were used in spectroscopic and structural analyses and reactivity studies. The ESI MS of **1** exhibits a prominent ion peak at a mass-to-charge (*m*/*z*) ratio of 318.0 (see Supplementary Fig. S3A), whose mass and isotope distribution pattern correspond to $[Ni(12\text{-}TMC)(O_2)]^+$ (calculated *m*/*z* of 318.2) (see Supplementary Fig. S3A, inset). When the reaction was carried out with isotopically labeled $H_2{}^{18}O_2$, a mass peak corresponding to $[Ni(12\text{-}TMC)(^{18}O_2)]^+$ appeared at *m*/*z* of 322.0 (calculated *m*/*z* of 322.2) (see Supplementary Fig. S3A, inset). The 4-mass unit upshift upon the substitution of ^{16}O with ^{18}O indicates that **1** contains an O_2 unit. The EPR spectrum of a frozen acetonitrile solution of **1** measured at 4.3 K exhibits a rhombic signal with *g* values of 2.22, 2.17 and 2.06 (see Supplementary Fig. S3B), which is indicative of a $(d_z{}^2)^1$ electron configuration typically observed for Ni(III) species[28], Ni(II)-superoxo complexes[24-26], and a six-coordinated bis(μ-superoxo)Ni_2(II) complex[29]. The room temperature magnetic moment of

2.13 μ_B, determined using the ^{1}H NMR Evans method[30], is consistent with an S = 1/2 ground state of **1**.

The resonance Raman spectrum of **1** was collected using 442-nm excitation at −20 °C. **1** prepared with $H_2{}^{16}O_2$ exhibits an isotopically sensitive band at 1002 cm^{-1} that shifts to 945 cm^{-1} when $H_2{}^{18}O_2$ is used, consistent with its assignment as an O-O stretching vibration on the basis of its $^{16}\Delta-{}^{18}\Delta$ value of 57 cm^{-1} ($^{16}\Delta-{}^{18}\Delta$ (calcd) = 57 cm^{-1}) (Fig. 1, inset). Interestingly, the observed O-O stretching frequency (1002 cm^{-1}) of **1** is significantly lower than that (1131 cm^{-1}) of **2**[25], but is between the superoxo (i.e., ν_{OO} of ~1050–1200 cm^{-1}) and peroxo (i.e., ν_{OO} of ~800–930 cm^{-1}) categories[31]. It is worth noting that the O-O stretching frequency (1002 cm^{-1}) of **1** is quite close to those observed in Cu(III)-peroxo species (~970 cm^{-1})[18,22]. Thus, the resonance Raman spectroscopic data suggests that the O_2 in **1** has significant peroxo character, $O_2{}^{2-}$.

The X-ray crystal structure of **1**-$(ClO_4)\cdot CH_3CN$ revealed the mononuclear side-on 1:1 nickel complex of O_2 in a distorted octahedral geometry arising from the triangular NiO_2 moiety with a small bite angle of 43.04(11)° (Fig. 2). Notably, the O-O bond length (1.386(4) Å) of **1** is longer than those of Ni(II)-superoxo complexes, such as **2** (1.301 Å, from DFT calculations)[25] and Ni(II)(O_2) with a β-diketiminato ligand (1.347 Å)[26]; the O-O bond length of **1** is between those of metal-superoxo compounds (~1.2–1.3 Å) and metal-peroxo compounds (~1.4–1.5 Å)[31], but closer to the metal-peroxo category. For comparison, the O-O bond length of 1.392 Å was reported in a Cu(III)-peroxo complex[22]. In addition, the Ni-O average bond of **1** (1.889 Å) is shorter than that of **2** (1.984 Å, from DFT calculations)[25], supporting a Ni(III) formulation. In conjunction with the low O-O stretching frequency measured by Raman spectroscopy, the structural data, such as O-O and Ni-O bond distances, suggest that **1** can be formulated as a Ni(III)-peroxo species, Ni(III)-($O_2{}^{2-}$).

Ni K-edge X-ray absorption spectroscopy was then performed to directly probe the oxidation state of nickel and the ligand field (LF) of the nickel center. The normalized Ni K-edge X-ray absorption spectra of **1** and **2** are presented in Fig. 3. The inset shows the expanded pre-edge region. The pre-edge features are due to an electric dipole-forbidden quadrupole-allowed 1s→3d transition[32]. The energy position of the pre-edge transition is dominantly affected by changes in LF at the absorbing Ni center and increases with increase in LF[23]. The pre-edge transitions in **1** and **2** occur at 8332.3 eV and 8331.6 eV, respectively, indicating an increase in LF on going from **2** to **1** (Fig. 3). The Ni K-edge energy position increases with increase in Q_{Ni}, the charge on the absorbing Ni center in the complex. Typically, for Ni complexes, the K-edge first-maxima do not show a large change with change in Q_{Ni}[33]; however, as seen in Fig. 3 the first-maximum is shifted ~1.8 eV in going from **2** to **1**, clearly indicating an increase in Q_{Ni} in **1** compared to **2**. Ni K-edge EXAFS data and their analyses show that the first shell coordination has increased from 5 in **2** to 6 in **1** (see Supplementary Figs. S4–S6, Tables S3 and S4), yet the Ni-O bond distance is ~0.06 Å shorter in **1** than in **2**. Together, the Ni K-edge and EXAFS data support a unique Ni(III)-($O_2{}^{2-}$) description for **1**. These data combined with the crystal structure indicate that the O_2 binds side-on to the Ni center in **1**, whereas the O_2 is end-on bound in **2** as previously reported[25]. This binding mode difference is accompanied by an electronic structure change from Ni(II)-($O_2{}^{-}$) in **2** to Ni(III)-($O_2{}^{2-}$) in **1**.

Density functional theory (DFT) calculations were performed to understand the role of the macrocyclic ring in determining the geometric and electronic structures of **1** and **2** (see Supplementary Fig. S7 and Table S5 for structural details). The geometry optimized structures of **1** and **2** show that the smaller 12-membered ring in **1** leads to contraction of the trans Ni-N bond angles. This displaces the Ni out of the $N_1N_2N_3N_4$ plane and allows for its facile side-on overlap with the O_2. The side-on coordination of the O_2 in **1** allows for a

stronger overlap of its π* orbital with the Ni $3d_x^2$-$_y^2$ orbital. This stronger σ overlap leads to the relative destabilization of the Ni $3d_x^2$-$_y^2$ orbital, transfers charge from the Ni $3d_x^2$-$_y^2$ orbital to the O_2, and results in a stable Ni(III)-(O_2^{2-}) species. We therefore conclude, based on the spectroscopic results, X-ray crystallography, and DFT calculations, that **1** is best described as a mononuclear Ni(III)-peroxo complex. The role of the supporting ligand, 12-TMC, is to sterically allow O_2 to bind in a side-on fashion, resulting in more sigma anti bonding with $3d_x^2$-$_y^2$ orbital as indicated above. It also stabilizes the high oxidation state of Ni^{3+}, by the strong interaction of Ni-$N_{equatorial}$ bond (2.059 Å) in **1** compared to Ni-$N_{equatorial}$ bond (2.10 Å from DFT calculations) in **2** (see Supplementary Table S5). Thus, as discussed in the mononuclear Cu-O_2 chemistry[10-17,20-23], the geometric and electronic structures of Ni-O_2 species are modulated by the nature of supporting ligands (Fig. 4).

The activity of **2** was investigated in electrophilic and nucleophilic reactions. First, the electrophilic character of **1** was tested in the oxidation of PPh_3, thioanisole, and xanthene. Upon addition of the substrates to the reaction solution of **2** in CH_3CN at 25 °C, the intermediate remained intact without showing any absorption spectral changes, and product analysis of the reaction solutions revealed that no oxygenated products were formed in the reactions. These results demonstrate that **2** is not capable of conducting electrophilic oxidation under the reaction conditions. In contrast, Ni(II)-superoxo complexes have shown reactivities in electrophilic reactions, such as the oxidation of PPh_3[25,26] and xanthene[34]. The nucleophilic character of **1** was investigated in aldehyde deformylation, with precedents that metal(III)-peroxo complexes with heme and non-heme ligands react with aldehydes to give the corresponding deformylated products[6,35,36]. Upon addition of 2-phenylpropionaldehyde (2-PPA) to **1** in CH_3CN at 25 °C, the characteristic UV-vis absorption bands of **1** disappeared with a first-order decay profile (see Supplementary Fig. S8A), and pseudo-first-order rate constants increased proportionally with the aldehyde concentration (k_2 = 4.0 × 10^{-2} M^{-1} s^{-1} at 25 °C) (see Supplementary Fig. S8B). Similar results were obtained in the reactions of cyclohexanecarboxaldehyde (CCA) but with a faster rate (k_2 = 2.0 × 10^{-1} M^{-1} s^{-1} at −10 °C) (see Supplementary Fig. S9). Product analysis of the resulting solutions revealed the formation of acetophenone (92 % based on **1**) and cyclohexene (85 % based on **1**) in the reactions of 2-PPA and CCA, respectively. The reactivity of **1** was further investigated using substituted benzaldehydes with a series of electron-donating and -withdrawing substituents at the *para*-position of the phenyl group (*para*-Y-Ph-CHO; Y = Me, F, H, Br, Cl) (see Supplementary Fig. S10). A positive ρ^+ value of 6.1 in the Hammett plot was obtained that is consistent with the process involving nucleophilic character of the Ni(III)-O_2 unit in the oxidation of aldehydes.

More interestingly, we have observed a complete intermolecular O_2-transfer from **1** to different transition metal complexes, such as $[Mn(II)(14\text{-}TMC)]^{2+}$ (**4**) (Fig. 5). Addition of **4** to a solution of **1** afforded changes in the absorption spectrum which are consistent with transfer of the O_2 from **1** to **4**, thereby producing **3** and a manganese(III)-peroxo complex, $[Mn(III)(14\text{-}TMC)(O_2)]^+$ (**5**) (Fig. 6)[36]. Well-defined isosbestic points were observed at 416 and 687 nm in the titration reaction (Fig. 6). The intermolecular O_2-transfer from **1** to **4** was further confirmed by ESI MS of the reaction solution, in which the mass peak corresponding to **1** disappeared with a concomitant appearance of mass peaks corresponding to **3** and **5** (see Supplementary Fig. S11). When the O_2-transfer reaction was carried out under an $^{18}O_2$ atmosphere, the product **5** did not contain the isotopically labeled $^{18}O_2$ group, demonstrating that molecular oxygen was not involved in the peroxo-transfer reaction. Since the peroxo-transfer reaction was fast at 25 °C in CH_3CN, kinetic studies were performed in acetone at −50 °C. Upon addition of 10 equiv of **4** to the solution of **1**, **1** disappeared with a first-order decay profile (see Supplementary Fig. S12A). Pseudo-first-order fitting of the kinetic data allowed us to determine the k_{obs} value to be 1.7(2) × 10^{-3} s^{-1} at −50 °C (see Supplementary Fig. S12A, inset). The first-order rate constants increased proportionally with the

concentration of **4**, giving a second-order rate constant of 0.2 M^{-1} s^{-1} at −50 °C (see Supplementary Fig. S12B). The rates were dependent on reaction temperatures, from which a linear Eyring plot was obtained between −60 and −30 °C to give the activation parameters of $\Delta H^{\ddagger}$ = 49 kJ mol^{-1} and $\Delta S^{\ddagger}$ = −76 J mol^{-1} K^{-1} (see Supplementary Fig. S12C). The observed second order kinetics and significant negative entropy value support that a bimolecular mechanism is operating in the O_2-transfer reaction, where the formation of the $[(12\text{-TMC})Ni–O_2–Mn(14\text{-TMC})]^{3+}$ intermediate is presumed to be the rate-determining step (Fig. 5). Finally, we found that the reverse reaction, which is the peroxo-transfer from **5** to **3**, does not occur. In this section, we have shown the first example of the complete O_2-transfer between metal complexes. The observation of the complete O_2-transfer from a Ni(III)-peroxo complex to a Mn(II) complex is different from the behavior of other systems where the formation of homo- or hetero-dinuclear complexes comprising $[M_2(\mu\text{-}O)_2]^{n+}$, $[M_2(O_2)]^{n+}$, or $[MM'(\mu\text{-}O)_2]^{n+}$ cores in the reactions of mononuclear M-O_2 adducts (M = Cu and Ni) and a second metal complex, M or M′, is observed[18,24,37,38]. The formation of $(Porp)Fe^{III}\text{-}(O_2^{2-})\text{-}Cu^{II}(L)$ complexes has also been observed in the reactions of Fe(III)-peroxo porphyrins with Cu(II)(L) complexes as chemical models of cytochrome c oxidase[39]. Detailed mechanistic investigations are underway in this laboratory to elucidate the difference between the complete O_2-transfer and the O_2-bridged dinuclear formation occurring in the reactions of mononuclear M-O_2 and second metal complexes.

In conclusion, a mononuclear side-on Ni(III)-peroxo complex was successfully synthesized by varying the supporting ligand of the previously reported Ni(II)-superoxo complex (i.e., the ring-size of the macrocyclic ligand). Combined with the precedents of mononuclear Cu-O_2 intermediates[14,17,18], the present results highlight the importance of supporting ligands in determining geometric and electronic structures of mononuclear Ni-O_2 complexes (i.e., Ni(III)-peroxo vs Ni(II)-superoxo species). Whether other factors, such as solvents, influence the geometric and electronic structures of Ni-O_2 complexes will be the subject of future studies. The reactivities of Ni(III)-peroxo and Ni(II)-superoxo complexes were compared in electrophilic and nucleophilic reactions. In contrast to Ni(II)-superoxo complexes, which show reactivities in oxidative electrophilic reactions[24], the Ni(III)-peroxo complex is not reactive in electrophilic reactions but is capable of deformylating aldehydes through nucleophilic reactions. The observation of complete O_2-transfer between metal complexes is unprecedented; whether this is a general feature in other metal-O_2 adducts requires further experimental and computational study.

Methods

See experimental section in supplementary information for detailed experimental conditions and procedures, spectroscopic and kinetics analyses, and computational calculations.

Supplementary Material

Refer to Web version on PubMed Central for supplementary material.

Acknowledgments

The research was supported by KOSEF/MEST of Korea through the CRI and WCU (R31-2008-000-10010-0) Programs (W.N.), the Ministry of Education, Culture, Sports, Science and Technology of Japan through the Global COE program and Priority Area (No. 20050029) (T.O.), and NIH grant DK-31450 (E.I.S.). SSRL operations are funded by the Department of Energy, Office of Basic Energy Sciences. The SSRL Structural Molecular Biology program is supported by the National Institutes of Health, National Center for Research Resources, Biomedical Technology Program, and the Department of Energy, Office of Biological and Environmental Research.

References

1. Nam W. Dioxygen activation by metalloenzymes and models. Acc Chem Res 2007;40:465–465. and review articles in the special issue.
2. Unno M, Chen H, Kusama S, Shaik S, Ikeda-Saito M. Structural characterization of the fleeting ferric peroxo species in Myoglobin: experiment and theory. J Am Chem Soc 2007;129:13394–13395. [PubMed: 17929929]
3. Kovaleva EG, Lipscomb JD. Crystal structures of Fe^{2+} dioxygenase superoxo, alkylperoxo, and bound product intermediates. Science 2007;316:453–457. [PubMed: 17446402]
4. Prigge ST, Eipper BA, Mains RE, Amzel LM. Dioxgyen binds end-on to mononuclear copper in a precatalytic enzyme complex. Science 2004;304:864–867. [PubMed: 15131304]
5. Klotz IM, Kurtz DM Jr. Metal-dioxygen complexes. Chem Rev 1994;94:567–568. and review articles in the special issue.
6. Wertz DL, Valentine JS. Nucleophilicity of iron-peroxo porphyrin complexes. Struct Bonding 2000;97:37–60.
7. Girerd JJ, Banse F, Simaan AJ. Characterization and properties of non-heme iron peroxo complexes. Struct Bonding 2000;97:145–177.
8. Bakac A. Kinetic and mechanistic studies of the reactions of transition metal-activated oxygen with inorganic substrates. Coord Chem Rev 2006;250:2046–2058.
9. Hikichi S, Akita M, Moro-oka Y. New aspects of the cobalt-dioxygen complex chemistry opened by hydrotris(pyrazoly)borate ligands (Tp^R): unique properties of Tp^RCo-dioxygen complexes. Coord Chem Rev 2000;198:61–87.
10. Mirica LM, Ottenwaelder X, Stack TDP. Structure and spectroscopy of copper–dioxygen complexes. Chem Rev 2004;104:1013–1045. [PubMed: 14871148]
11. Lewis EA, Tolman WB. Reactivity of dioxygen-copper systems. Chem Rev 2004;104:1047–1076. [PubMed: 14871149]
12. Hatcher LQ, Karlin KD. Oxidant types in copper-dioxygen chemistry: the ligand coordination defines the Cu_n-O_2 structure and subsequent reactivity. J Biol Inorg Chem 2004;9:669–683. [PubMed: 15311336]
13. Itoh S. Mononuclear copper active-oxygen complexes. Curr Opin Chem Biol 2006;10:115–122. [PubMed: 16504568]
14. Cramer CJ, Tolman WB. Mononuclear Cu–O_2 complexes: geometries, spectroscopic properties, electronic structures, and reactivity. Acc Chem Res 2007;40:601–608. [PubMed: 17458929]
15. Rolff M, Tuczek F. How do copper enzymes hydroxylate aliphatic substrates? Recent insights from the chemistry of model systems. Angew Chem Int Ed 2008;47:2344–2347.
16. Chen P, Solomon EI. O_2 activation by binuclear Cu sites: noncoupled versus exchange coupled reaction mechanisms. Proc Natl Acad Sci USA 2004;101:13105–13110. [PubMed: 15340147]
17. Fujisawa K, Tanaka M, Moro-oka Y, Kitajima N. A monomeric side-on superoxocopper(II) complex: $Cu(O_2)(HB(3\text{-}tBu\text{-}5\text{-}iPrpz)_3)$. J Am Chem Soc 1994;116:12079–12080.
18. Spencer DJE, Aboelella NW, Reynolds AM, Holland PL, Tolman WB. β-Diketiminate ligand backbone structural effects on Cu(I)/O_2 reactivity: unique copper–superoxo and bis(μ-oxo) complexes. J Am Chem Soc 2002;124:2108–2109. [PubMed: 11878952]
19. Würtele C, et al. Crystallographic characterization of a synthetic 1:1 end-on copper dioxygen adduct complex. Angew Chem Int Ed 2006;45:3867–3869.
20. Gherman BF, Cramer CJ. Modeling the peroxide/superoxide continuum in 1:1 side-on adducts of O_2 with Cu. Inorg Chem 2004;43:7281–7283. [PubMed: 15530076]
21. Aboelella NW, et al. Dioxygen activation at a single copper site: structure, bonding, and mechanism of formation of 1:1 Cu-O_2 Adducts. J Am Chem Soc 2004;126:16896–16911. [PubMed: 15612729]
22. Reynolds AM, Gherman BF, Cramer CJ, Tolman WB. Characterization of a 1:1 Cu-O_2 adduct supported by an anilido imine ligand. Inorg Chem 2005;44:6989–6997. [PubMed: 16180861]

23. Sarangi R, et al. X-ray absorption edge spectroscopy and computational studies on $LCuO_2$ species: superoxide–Cu^{II} versus peroxide–Cu^{III} bonding. J Am Chem Soc 2006;128:8286–8296. [PubMed: 16787093]
24. Kieber-Emmons MT, Riordan CG. Dioxygen activation at monovalent nickel. Acc Chem Res 2007;40:618–625. [PubMed: 17518438]
25. Kieber-Emmons MT, et al. Identification of an “end-on” nickel–superoxo adduct, $[Ni(tmc)(O_2)]^+$ J Am Chem Soc 2006;128:14230–14231. [PubMed: 17076476]
26. Yao S, Bill E, Milsmann C, Wieghardt K, Driess M. A “side-on” superoxonickel complex $[LNi(O_2)]$ with a square-planar tetracoordinate nickel(II) center and its conversion into $[LNi(\mu\text{-}OH)_2NiL]$. Angew Chem Int Ed 2008;47:7110–7113.
27. Matsumoto M, Nakatsu K. Dioxygen-bis-(t-butylisocyanide)nickel. Acta Cryst 1975;B31:2711–2713.
28. Haines RI, McAuley A. Synthesis and reactions of nickel(III) complexes. Coord Chem Rev 1981;39:77–119.
29. Cho J, et al. Sequential reaction intermediates in aliphatic C–H bond fuctionalization initiated by a bis(μ-oxo)dinickel(III) complex. Inorg Chem 2006;45:2873–2885. [PubMed: 16562943]
30. Evans DF, Jakubovic DA. Water-soluble hexadentate Schiff-base lignads as sequestrating agents for iron(III) and gallium(III). J Chem Soc Dalton Trans 1988:2927–2933.
31. Cramer CJ, Tolman WB, Theopold KH, Rheingold AL. Varible character of O–O and M–O bonding in side-on (η^2) 1:1 metal complexes of O_2. Proc Natl Acad Sci USA 2003;100:3635–3640. [PubMed: 12634422]
32. Shulman RG, Yafet Y, Eisenberger P, Blumberg WE. Observation and interpretation of X-ray absorption edges in iron compounds and proteins. Proc Natl Acad Sci USA 1976;73:1384–1388. [PubMed: 5720]
33. Colpas GJ, et al. X-ray spectroscopic studies of nickel complexes, with application to the structure of nickel sites in hydrogenases. Inorg Chem 1991;30:920–928.
34. Nam W, et al. unpublished results.
35. Vaz ADN, Roberts ES, Coon MJ. Olefin formation in the oxidative deformylation of aldehydes by cytochrome P-450. Mechanistic implications for catalysis by oxygen-derived peroxide. J Am Chem Soc 1991;113:5886–5887.
36. Seo MS, et al. $[Mn(tmc)(O_2)]^+$: a side-on peroxido manganese(III) complex bearing a non-heme ligand. Angew Chem Int Ed 2007;46:377–380.
37. Kieber-Emmons MT, Schenker R, Yap GPA, Brunold TC, Riordan CG. Spectroscopic elucidation of a peroxo $Ni_2(\mu\text{-}O_2)$ intermediate derived from a nickel(I) complex and dioxygen. Angew Chem Int Ed 2004;43:6716–6718.
38. Aboelella NW, et al. Mixed metal bis(μ-oxo) complexes with $[CuM(\mu\text{-}O)_2]^{n+}$ (M = Ni(III) or Pd(II)) cores. Chem Commun 2004:1716–1717.
39. Chufán EE, Puiu SC, Karlin KD. Heme–copper/dioxygen adduct formation, properties, and reactivity. Acc Chem Res 2007;40:563–572. [PubMed: 17550225]

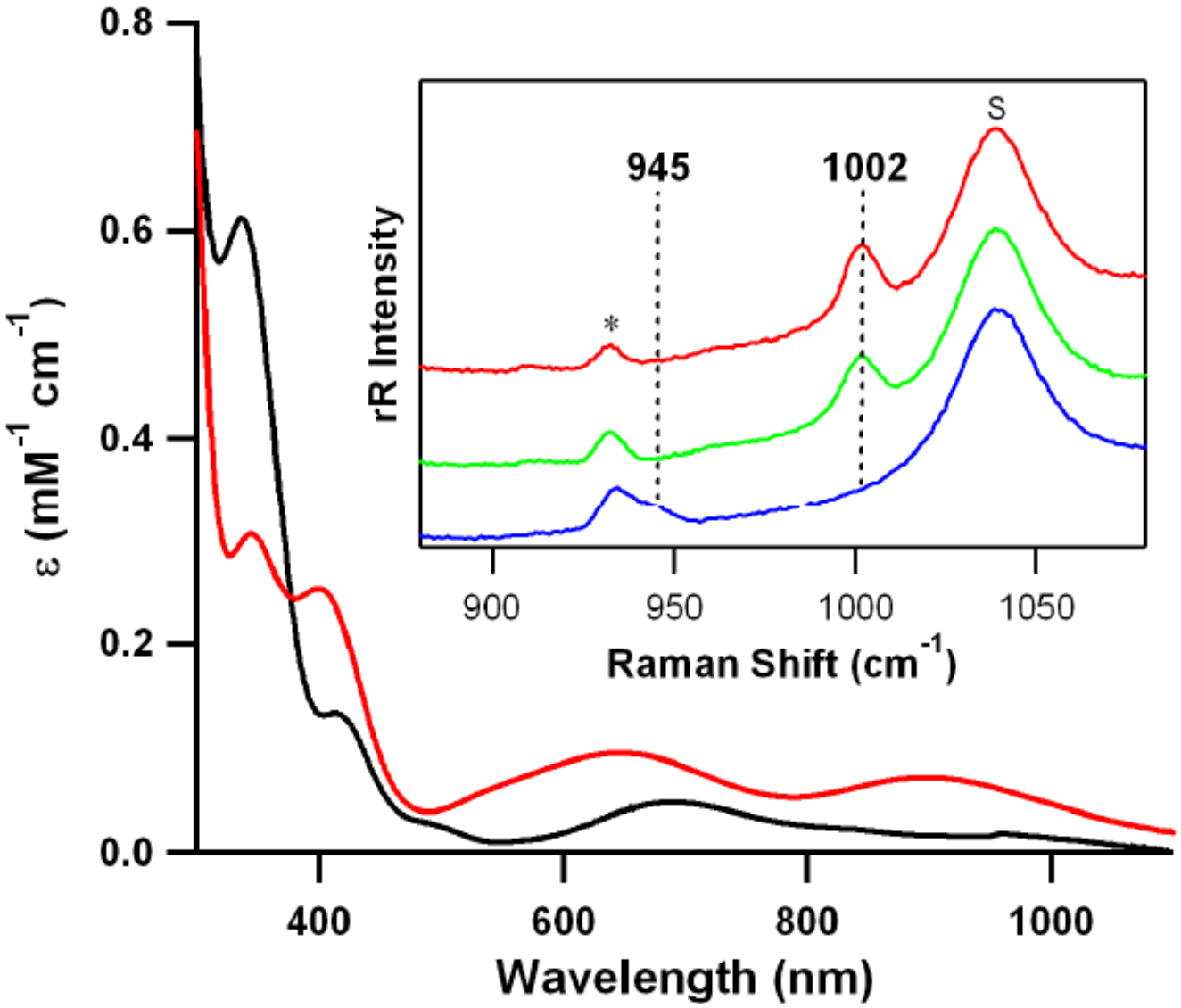

Figure 1. Characterization of 1

Electronic absorption spectra of **1** (red solid line) and **2** (black solid line) in CH_3CN at 0 °C. Inset shows resonance Raman spectra of **1** (32 mM) obtained upon excitation at 442 nm in CD_3CN at −20 °C; isolated **1** (red line) and in situ-generated **1** prepared with $H_2{}^{16}O_2$ (green line) and $H_2{}^{18}O_2$ (blue line). The peak marked with "s" is ascribed to d_3-acetonitrile solvent and an asterisk denotes a band derived from a nickel complex bearing 12-TMC ligand.

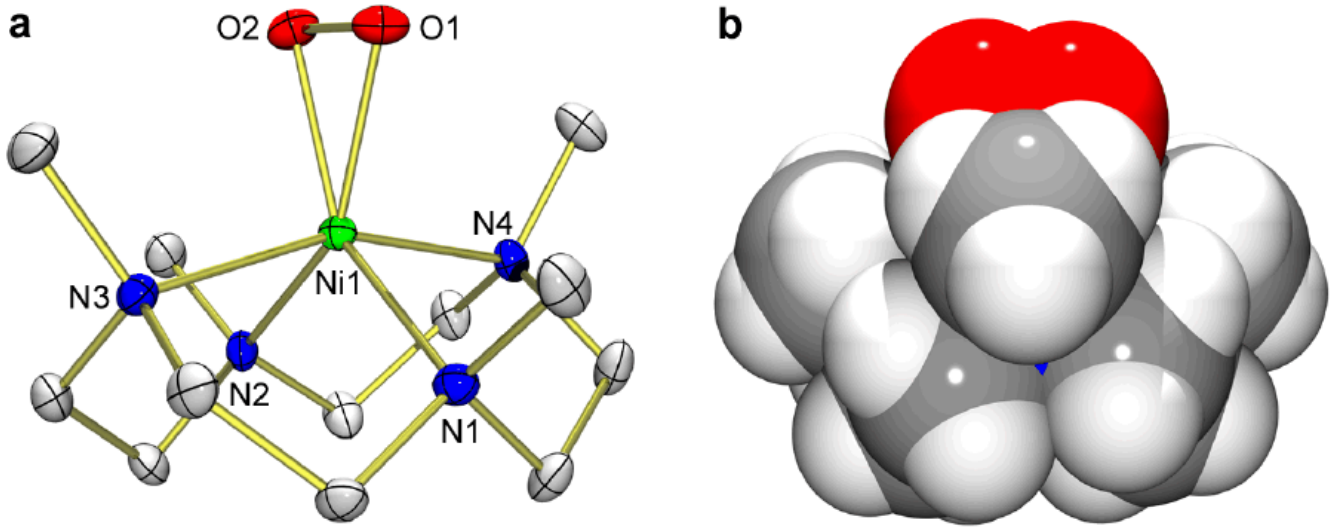

Figure 2. X-ray crystal structure of 1

a, ORTEP plot of $[Ni(12\text{-}TMC)(O_2)]^+$ (**1**) with thermal ellipsoids drawn at the 30 % probability level. Hydrogen atoms are omitted for clarity. **b,** Side view (space-filling representation) of **1**, derived from the crystal structure determination. Selected bond lengths (Å) and angles (°): Ni-O1 1.884(3), Ni-O2 1.894(3), Ni-N1 2.027(3), Ni-N2 2.038(3), Ni-N3 2.160(3), Ni-N4 2.158(3), O1-O2 1.386(4); O1-Ni-O2 43.04(11), Ni-O1-O2 68.87(16), Ni-O2-O1 68.09(15). The crystallographic data have been deposited with the Cambridge Crystallographic Data Center under CCDC 719999.

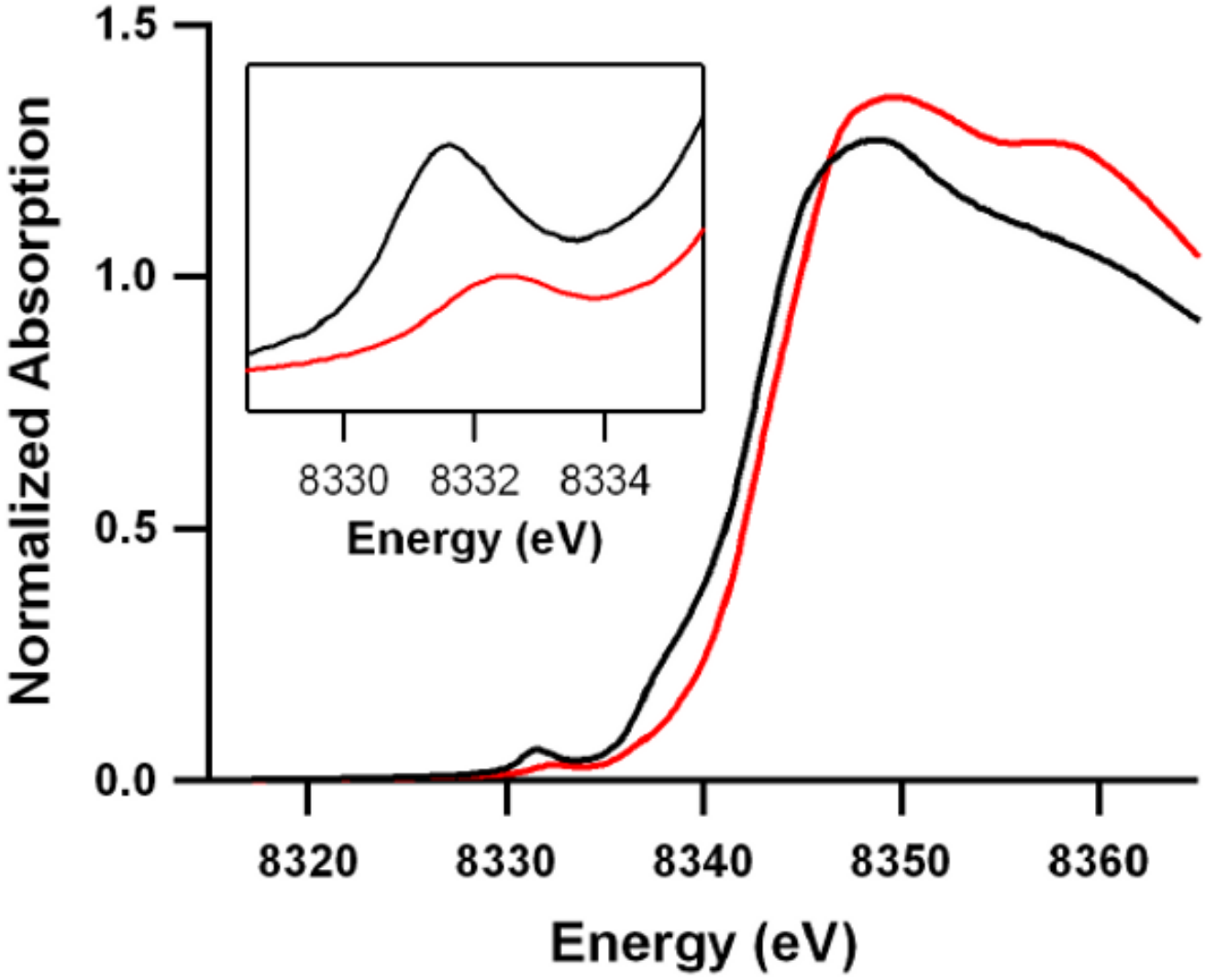

Figure 3. Ni K-edge x-ray absorption spectra of 1 (–) and 2 (–)

The inset shows the expanded pre-edge region. The Ni K-edge XAS spectrum of **2** was reported previously in [ref. 18]. Due to large differences in the beamline optics, cryostat temperatures, and detection methods, the data were re-measured in the present study for accurate comparison of **1** and **2** under identical conditions.

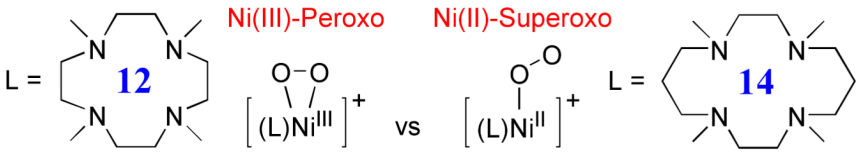

Figure 4. Formation of Ni(III)-peroxo vs Ni(II)-superoxo intermediates

The geometric and electronic structures of Ni-O_2 intermediates are determined by the ring-size of macrocyclic ligands, such as a Ni(III)-peroxo complex with a 12-membered macrocyclic ligand and a Ni(II)-superoxo complex with a 14-membered macrocyclic ligand.

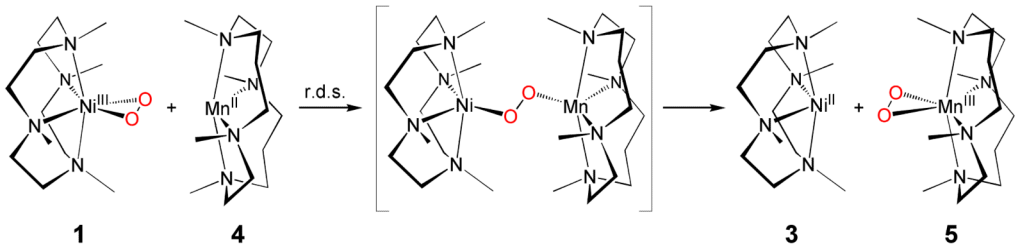

Figure 5. Reaction scheme showing an intermolecular O_2-transfer between metal complexes

An O_2 group is transferred from $[Ni(III)(12\text{-}TMC)(O_2)]^+$ (**1**) to $[Mn(II)(14\text{-}TMC)]^{2+}$ (**4**) via a $[(12\text{-}TMC)Ni–O_2–Mn(14\text{-}TMC)]^{3+}$ transition state, and the final products are $[Ni(II)(12\text{-}TMC)]^{2+}$ (**3**) and $[Mn(III)(14\text{-}TMC)(O_2)]^+$ (**5**).

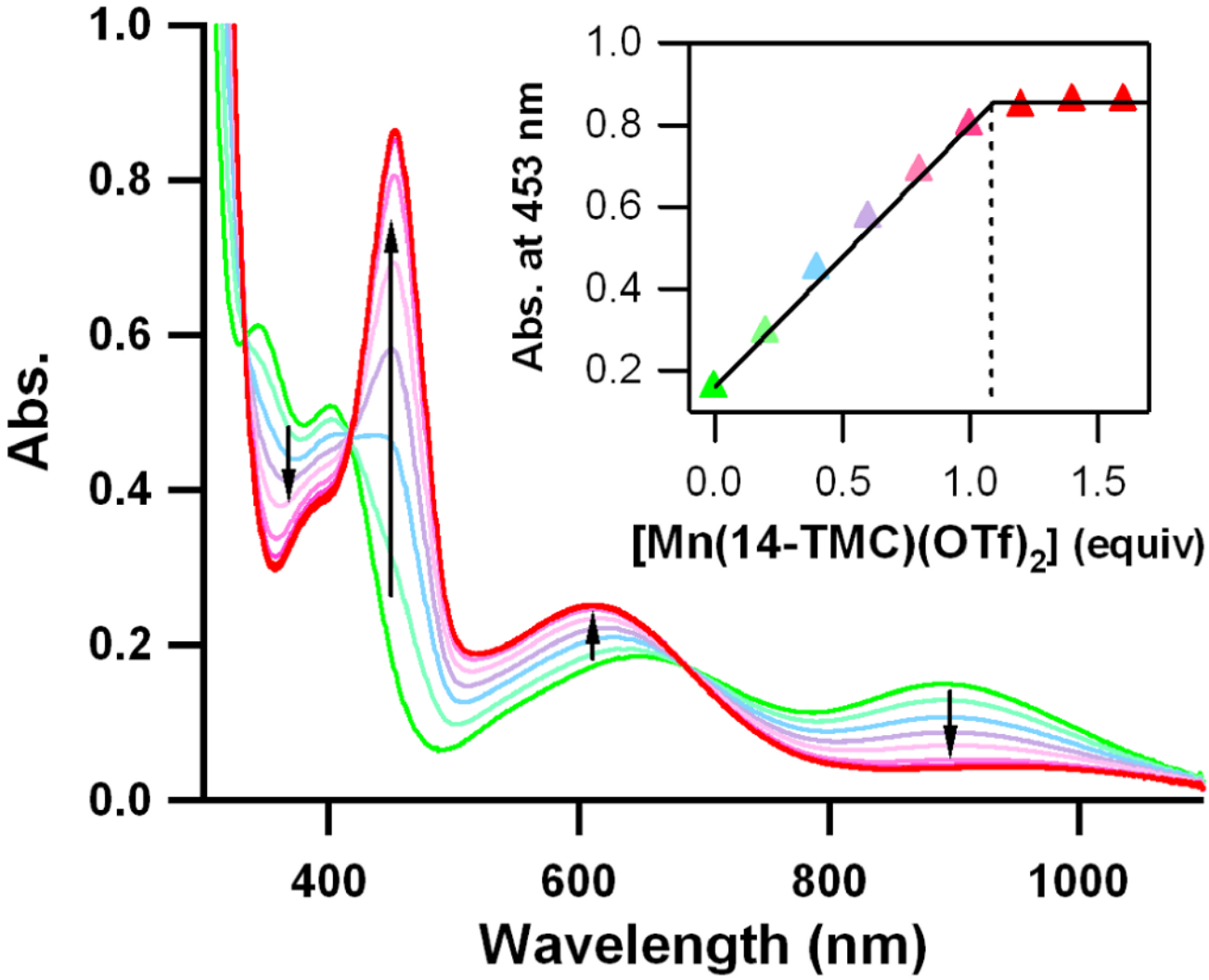

Figure 6. Spectral evidence for an intermolecular O_2-transfer from 1 to 4

UV-vis spectral changes showing the formation of $[Mn(14\text{-}TMC)(O_2)]^+$ (**5**) (red) and the disappearance of $[Ni(III)(12\text{-}TMC)(O_2)]^+$ (**1**) (green) by addition of $[Mn(II)(14\text{-}TMC)]^{2+}$ (**4**) to a solution of **1** in increments of 0.2 equiv in CH_3CN at 25 °C. Inset shows the spectroscopic titration at 453 nm for the formation of **5** as a function of the equiv of **4** added to a solution of **1** in increments of 0.2 equiv.